

## LUMINOSITY EVOLUTION OF GAMMA-RAY PULSARS

KOUICHI HIROTANI<sup>1</sup>

Theoretical Institute for Advanced Research in Astrophysics (TIARA), Academia Sinica, Institute of Astronomy and Astrophysics (ASIAA), PO Box 23-141, Taipei, Taiwan

Received 2012 November 19; accepted 2013 January 22

### ABSTRACT

We investigate the electrodynamic structure of a pulsar outer-magnetospheric particle accelerator and the resultant gamma-ray emission. By considering the condition for the accelerator to be self-sustained, we derive how the trans-magnetic-field thickness of the accelerator evolves with the pulsar age. It is found that the thickness is small but increases steadily if the neutron-star envelope is contaminated by sufficient light elements. For such a light element envelope, the gamma-ray luminosity of the accelerator is kept approximately constant as a function of age in the initial ten thousand years, forming the lower bound of the observed distribution of the gamma-ray luminosity of rotation-powered pulsars. If the envelope consists of only heavy elements, on the other hand, the thickness is greater but increases less rapidly than what a light element envelope has. For such a heavy element envelope, the gamma-ray luminosity decreases relatively rapidly, forming the upper bound of the observed distribution. The gamma-ray luminosity of a general pulsar resides between these two extreme cases, reflecting the envelope composition and the magnetic inclination angle with respect to the rotation axis. The cutoff energy of the primary curvature emission is regulated below several GeV even for young pulsars, because the gap thickness, and hence the acceleration electric field is suppressed by the polarization of the produced pairs.

*Subject headings:* gamma rays: stars — magnetic fields — methods: analytical — methods: numerical  
 — stars: neutron

### 1. INTRODUCTION

The Large Area Telescope aboard *Fermi Gamma-ray Space Telescope* (Atwood et al. 2009) has proved remarkably successful at discovering rotation-powered pulsars emitting photons above 0.1 GeV. Thanks to its superb sensitivity, the number of gamma-ray pulsars has increased from six in Compton Gamma Ray Observatory era (Thompson 2004) to more than one hundred (Nolan 2012). Plotting their best estimate of the gamma-ray luminosity,  $L_\gamma$ , against the spin-down luminosity,  $L_{\text{spin}} = 4\pi^2 \dot{I} P^{-3}$ , Abdo et al. (2010) found the important relation that  $L_\gamma$  is approximately proportional to  $L_{\text{spin}}^{0.5}$  (with a large scatter), where  $I$  refers to the neutron-star (NS) moment of inertia,  $P$  the NS rotational period, and  $\dot{P}$  its temporal derivative. However, it is unclear why this relationship arises, in spite of its potential importance to discriminate pulsar emission models such as the polar-cap model (Harding et al. 1978; Daugherty & Harding 1982; Dermer 1994), the outer-gap model (Chiang & Romani 1992; Romani 1996; Zhang & Cheng 1997; Takata et al. 2004; Hirotani 2008; Wang et al. 2011), the pair-starved polar-cap model (Venter et al. 2009) (see also Yuki & Shibata (2012) for the possible co-existence of such models), and the emission model from the wind zone (Petri 2011; Bai & Spitkovski 2010a,b; Aharonian et al. 2012).

Recent gamma-ray observations suggest that the pulsed gamma-rays are emitted from the higher altitudes of a pulsar magnetosphere. This is because the

observed light curves (Abdo et al. 2010) favor fan-like emission geometry, which scan over a large fraction of the celestial sphere, and because the Crab pulsar shows pulsed photons near and above 100 GeV (Aliu et al. 2011; Aleksić et al. 2011a,b), which rules out an emission from the lower altitudes, where strong magnetic absorption takes place for  $\gamma$ -rays above 10 GeV. Consequently, higher-altitude emission models such as the outer-gap model (Cheng et al. 1986a,b), the high-altitude slot-gap model (Muslimov & Harding 2004), or the pair-starved polar-cap model (Venter et al. 2009), gathered attention. It is noteworthy that the outer-gap model is presently the only higher-altitude emission model that is solvable from the basic equations self-consistently (Hirotani 2011a). In the present paper, therefore, we focus on the outer-gap model and derive the observed relationship  $L_\gamma \propto L_{\text{spin}}^{0.5}$  both analytically and numerically.

We schematically depict the pulsar outer-magnetospheric accelerator (i.e., the outer gap) in figure 1. As the NS rotates, there appears the light cylinder, within which plasmas can co-rotate with the magnetosphere. The magnetic field lines that become tangential to the light cylinder at the light cylinder radius,  $\varpi_{\text{LC}} = cP/2\pi$ , are called the last-open magnetic field lines, where  $c$  refers to the speed of light. Pairs are produced via photon-photon pair production mostly near the null-charge surface and quickly polarized by the magnetic-field-aligned electric field,  $E_\parallel$ , in the gap. In this paper, we assume that the rotation and magnetic axes reside in the same hemisphere to obtain  $E_\parallel > 0$ , which accelerates positrons ( $e^+$ 's) outwards while electrons ( $e^-$ 's) inwards. These ultra-relativistic particles have Lorentz factors,  $\gamma \sim 10^{7.5}$ , to emit

<sup>1</sup> Postal address: TIARA, Department of Physics, National Tsing Hua University, 101, Sec. 2, Kuang Fu Rd., Hsinchu, Taiwan 300

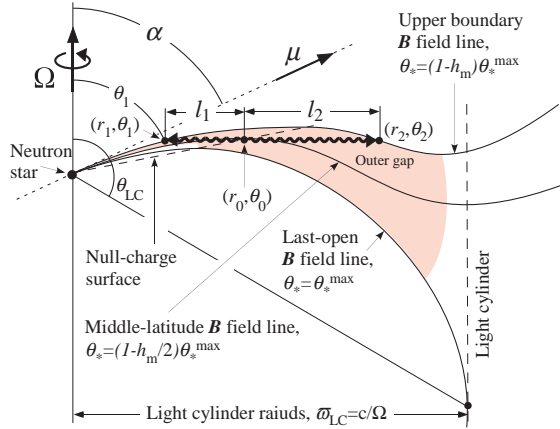


FIG. 1.— Side view of an outer gap. The neutron star (filled circle on the left) obliquely rotates around the vertical axis with magnetic inclination angle  $\alpha$ . The thin solid curves denote the magnetic field lines, while the dashed straight line the null-charge surface, on which the magnetic field lines become perpendicular to the rotation axis. Outside the light cylinder (the vertical long dashed line), plasmas that are frozen to the magnetic field lines can only migrate outwards (as a pulsar wind) because of the causality requirement in special relativity. The light-cylinder radius,  $\varpi_{LC}$ , becomes typically a few or several hundred neutron-star radii for young pulsars. In modern outer-gap models (Hirotani et al. 2003; Takata et al. 2004; Hirotani 2006a; Takata et al. 2004), it is proved that the outer gap extends between the stellar surface (because of a negative charge density in the lower altitudes) and the vicinity of the light cylinder (because of a positive charge density in the higher altitudes). Thus, typical inward (or outward) photons propagate distance  $l_1$  (or  $l_2$ ) before escaping from the gap (shaded region).

photons efficiently by the curvature process.

## 2. ANALYTICAL EXAMINATION OF OUTER-GAP LUMINOSITY

In this section, we analytically derive how the gamma-ray luminosity of an outer gap evolves with time. In the outer magnetosphere, only the dipole component remains in the magnetic field; thus, the inhomogeneous part of the Maxwell equation (i.e., the Poisson equation for the electro-static potential) gives the magnetic-field-aligned electric field (Hirotani 2008),

$$E_{\parallel} \approx \frac{\mu}{2\varpi_{LC}^3} h_m^2, \quad (1)$$

where  $\mu$  denotes the NS magnetic dipole moment, and  $h_m$  the trans-magnetic-field thickness of the gap. Since the Poisson equation is a second-order differential equation,  $E_{\parallel}$  is proportional to  $h_m^2$ . Electrons ( $e^-$ 's) and positrons ( $e^+$ 's) are created via photon-photon (and sometimes via magnetic) pair production, being subsequently polarized by  $E_{\parallel}$  and accelerated in the opposite directions, to finally attain the terminal Lorentz factor

$$\gamma = \left( \frac{3\rho_c^2 E_{\parallel}}{2e} \right)^{1/4}, \quad (2)$$

where  $\rho_c$  refers to the radius of curvature of particle's motion in the three-dimensional magnetosphere,  $e$  the charge on the positron. Photons are radiated by such ultra-relativistic  $e^{\pm}$ 's via curvature process with characteristic energy,

$$h\nu_c = \frac{3}{2} \hbar c \frac{\gamma^3}{\rho_c}, \quad (3)$$

where  $h$  denotes the Planck constant,  $\hbar \equiv h/2\pi$ . Once  $h_m$  is obtained, we can readily compute the  $\gamma$ -ray luminosity of curvature radiation from an outer gap by (Hirotani 2008)

$$L_{\gamma} \approx 2.36(\nu F_{\nu})_{\text{peak}} \times 4\pi d^2 f_{\Omega} \approx 1.23 f_{\Omega} h_m^3 \frac{\mu^2 \Omega^4}{c^3}, \quad (4)$$

where  $f_{\Omega}$ , which has been conventionally assumed to be approximately unity, refers to the flux correction factor (Romani, R. & Watters 2010), and  $\Omega = 2\pi/P$  the rotation angular frequency of the NS. Here, it is assumed that the current density flowing in the gap is comparable to the Goldreich-Julian value (Goldreich, & Julian 1969). The last factor,  $\mu^2 \Omega^4 / c^3$  is proportional to the spin-down luminosity,  $L_{\text{spin}}$ . Therefore, the evolution law,  $L_{\gamma} \propto L_{\text{spin}}^{0.5}$ , is crucially governed by the evolution of  $h_m$  as a function of the NS age,  $t$ .

The evolution of  $h_m$  is essentially controlled by the photon-photon pair production in the pulsar magnetosphere. To analytically examine the pair production, we assume the static dipole magnetic field configuration for simplicity, and consider the plane on which both the rotational and magnetic axes reside (fig. 1). On this two-dimensional latitudinal plane, the last-open field line intersects the NS surface at magnetic co-latitudinal angle  $\theta_*^{\text{max}}$  (measured from the magnetic dipole axis) that satisfies

$$\frac{\sin^2 \theta_*^{\text{max}}}{r_*} = \frac{\sin^2(\theta_{LC} - \alpha)}{\varpi_{LC} / \sin \theta_{LC}}, \quad (5)$$

where  $r_*$  denotes the NS radius,  $\theta_{LC}$  the angle (measured from the rotation axis) of the point where the last-open field line becomes tangential to the light cylinder, and  $\alpha$  the inclination angle of the dipole magnetic axis with respect to the rotation axis. A magnetic field line can be specified by the magnetic co-latitude (measured from the dipole axis),  $\theta_*$ , where it intersects the stellar surface. A magnetic field line does not close within the light cylinder (i.e., open to large distances) if  $0 < \theta_* < \theta_*^{\text{max}}$ . Thus, the last-open field lines,  $\theta_* = \theta_*^{\text{max}}$ , corresponds to the *lower* boundary, which forms a surface in a three-dimensional magnetosphere, of the outer gap.

Let us assume that the gap *upper* boundary coincides with the magnetic field lines that are specified by  $\theta_* = (1 - h_m)\theta_*^{\text{max}}$ . Numerical examinations show that  $h_m$ , indeed, changes as a function of the distance along the field line and the magnetic azimuthal angle (measured counter-clockwise around the dipole axis). Nevertheless, except for young pulsars like the Crab pulsar, an assumption of a spatially constant  $h_m$  gives a relatively good estimate. Thus, for an analytical purpose, we adopt a constant  $h_m$  in this analytical examination. In this case, we can specify the middle-latitude field line by the magnetic co-latitude  $\theta_* = (1 - h_m/2)\theta_*^{\text{max}}$ . Screening of  $E_{\parallel}$  due to the polarization of the produced pairs, takes place mostly in the lower altitudes. It is, therefore, appropriate to evaluate the screening of  $E_{\parallel}$  around the point  $(r_0, \theta_0)$  where the null-charge surface intersects the middle-latitude field line (fig. 1).

An inwardly migrating electron (or an outwardly migrating positron) emits photons inwards (or outwards), which propagate the typical distance  $l_1$  (or  $l_2$ ) before escaping from the gap. Denoting the cross section of the

inward (or outward) horizontal line from the point  $(r_0, \theta_0)$  and the upper boundary as  $(r_1, \theta_1)$  (or as  $(r_2, \theta_2)$ ), and noting  $r_0 \cos \theta_0 = r_1 \cos \theta_1 = r_2 \cos \theta_2$ , we obtain

$$l_1 = r_0 \cos \theta_0 (\tan \theta_0 - \tan \theta_1), \quad (6)$$

$$l_2 = r_0 \cos \theta_0 (\tan \theta_2 - \tan \theta_0). \quad (7)$$

Along the upper-boundary field line, we obtain

$$\frac{\sin^2(\theta_1 - \alpha)}{r_1} = \frac{\sin^2(\theta_2 - \alpha)}{r_2} = \frac{\sin^2[(1 - h_m)\theta_*^{\max}]}{r_*}, \quad (8)$$

whereas along the middle-latitude field line, we obtain

$$\frac{\sin^2(\theta_0 - \alpha)}{r_0} = \frac{\sin^2[(1 - h_m/2)\theta_*^{\max}]}{r_*}. \quad (9)$$

Combining these two equations, and noting  $\theta_*^{\max} \ll 1$ , we find that  $\theta_1 (< \theta_0)$  and  $\theta_2 (> \theta_0)$  can be given by the solution  $\theta$  that satisfies

$$\cos \theta \sin^2(\theta - \alpha) = \left( \frac{1 - h_m}{1 - h_m/2} \right)^2 \cos \theta_0 \sin^2(\theta_0 - \alpha), \quad (10)$$

where  $\theta_0$  is given by

$$\tan \theta_0 = \frac{1}{2} \left( 3 \tan \alpha + \sqrt{9 \tan^2 \alpha + 8} \right). \quad (11)$$

Thus, if we specify  $\alpha$ , we can solve  $\theta = \theta_1$  and  $\theta = \theta_2$  as a function of  $h_m$  by equation (10). Substituting these  $\theta_1$  and  $\theta_2$  into equations (6) and (7), we obtain  $l_1$  and  $l_2$ , where  $r_0$  depends on  $P$ .

If  $h_m \ll 1$ , we can expand the left-hand side of equation (10) around  $\theta = \theta_0$ , where  $\theta = \theta_1$  for inward (or  $\theta = \theta_2$  for outward)  $\gamma$ -rays to find  $\theta_2 - \theta_0 = \theta_0 - \theta_1 \propto \sqrt{h_m}$ . That is, the leading terms in the expansion vanish and we obtain  $l_1 = l_2$  from the next-order terms, which are quadratic to  $\theta - \theta_0$ . Assuming  $L_X \propto t^{-\beta}$ , where  $\beta \approx 0.48$  is appropriate for  $t < 10^4$  years for a light-element-envelope NS and for  $t < 10^5$  years for a heavy-element NS, we find  $h_m \propto P^{5/6} \mu^{-1/6} t^{\beta/2}$ , and hence  $L_\gamma \propto P^{-3/2} \mu^{3/2} t^{3\beta/2}$ . Since the dipole radiation formula gives  $P \propto \mu t^{1/2}$ , we obtain  $L_\gamma \propto \mu^0 t^{3(\beta-1/2)/2} \propto t^{-0.03}$ . Thus, when the gap is very thin, which is expected for a light-element-envelope NS,  $L_\gamma$  little evolves with the pulsar age,  $t$ .

However, if  $h_m > 0.2$ , say, the rapidly expanding magnetic flux tube gives asymmetric solution,  $l_2 > l_1$ . That is, the third and higher order terms in the expansion contribute significantly compared to the quadratic terms. Thus, we must solve equation (10) for  $\theta$  ( $= \theta_1$  or  $\theta_2$ ) without assuming  $|\theta - \theta_0| \ll 1$ , in general.

Let us now consider the condition for a gap to be self-sustained. A single ingoing  $e^-$  or an outgoing  $e^+$  emits

$$(N_\gamma)_1 = eE_\parallel l_1 / (h\nu_c) \quad (12)$$

or

$$(N_\gamma)_2 = eE_\parallel l_2 / (h\nu_c) \quad (13)$$

photons while running the typical distance  $l_1$  or  $l_2$ , respectively. Such photons materialize as pairs with probability

$$\tau_1 = l_1 F_1 \sigma_1 / c \quad (14)$$

or

$$\tau_2 = l_2 F_2 \sigma_2 / c, \quad (15)$$

where  $F_1$  and  $F_2$  denote the X-ray flux inside and outside of  $(r_0, \theta_0)$ , respectively;  $\sigma_1$  and  $\sigma_2$  are the pair-production cross section for inward and outward photons, respectively. Thus, a single  $e^-$  or  $e^+$  cascades into

$$(N_\gamma)_1 \tau_1 = \frac{eE_\parallel}{h\nu_c} \frac{F_1}{c} l_1^2 \sigma_1 \quad (16)$$

pairs or into

$$(N_\gamma)_2 \tau_2 = \frac{eE_\parallel}{h\nu_c} \frac{F_2}{c} l_2^2 \sigma_2 \quad (17)$$

pairs within the gap. That is, a single inward-migrating  $e^-$  cascades into pairs with multiplicity  $(N_\gamma)_1 \tau_1$ . Such produced pairs are polarized by  $E_\parallel$ . Each returning, outward-migrating  $e^+$  cascades into pairs with multiplicity  $(N_\gamma)_2 \tau_2$  in outer magnetosphere. As a result, a single inward  $e^-$  cascades eventually into  $(N_\gamma)_1 \tau_1 \cdot (N_\gamma)_2 \tau_2$  inward  $e^-$ 's, which should become unity for the gap to be self-sustained. Therefore, in a stationary gap, the gap thickness  $h_m$  is automatically regulated so that the gap closure condition,

$$(N_\gamma)_1 \tau_1 \cdot (N_\gamma)_2 \tau_2 = 1, \quad (18)$$

may be satisfied.

Approximately speaking, a single, inward-migrating  $e^-$  emits  $(N_\gamma)_1 \sim 10^4$  curvature photons, a portion of which head-on collide the surface X-ray photons to materialize as pairs with probability  $\tau_1 \sim 10^{-3}$  within the gap. Thus, a single  $e^-$  cascades into  $(N_\gamma)_1 \tau_1 \sim 10$  pairs in the gap. Each produced  $e^+$  return outwards to emit  $(N_\gamma)_2 \sim 10^5$  photons, which materialize as pairs with probability  $\tau_2 \sim 10^{-6}$  by tail-on colliding with the surface X-rays. In another word,  $(N_\gamma)_1 \tau_1 \sim 10$  holds regardless of the nature of the pair production process (e.g., either photon-photon or magnetic process (Takata et al. 2010)) in the lower altitudes, because it is determined by the pair-production efficiency in the outer magnetosphere  $(N_\gamma)_2 \tau_2 \sim 0.1$ , which is always due to photon-photon pair production.

In general,  $(N_\gamma)_1$ ,  $\tau_1$ ,  $(N_\gamma)_2$ ,  $\tau_2$  are expressed in terms of  $h_m$ ,  $P$ ,  $\mu$ ,  $T$ , and  $\alpha$ , where  $T$  denotes the NS surface temperature. Note that we can solve  $P = 2\pi/\Omega$  as a function of the NS age,  $t$ , from the spin-down law. Thus, specifying  $\alpha$  and the cooling curve,  $T = T(t)$ , we can solve  $h_m$  as a function of  $t$  from the gap closure condition,  $(N_\gamma)_1 \tau_1 (N_\gamma)_2 \tau_2 = 1$ . Note also that the spin-down law readily gives the spin-down luminosity,  $L_{\text{spin}} \propto \dot{P} P^{-3}$ , as a function of  $t$ , once  $P = P(t, \alpha)$  is solved. On these grounds,  $L_\gamma$  can be related to  $L_{\text{spin}}$  with an intermediate parameter  $t$ , if we specify the cooling curve and the spin-down law.

Substituting equations (16) and (17) into (18), we obtain

$$\frac{eE_\parallel}{h\nu_c} \frac{\sqrt{F_1 \sigma_1 F_2 \sigma_2}}{c} l_1 l_2 = 1, \quad (19)$$

where

$$F_i \sigma_i = \pi(1 - \mu_i) \left( \frac{r_*}{r_i} \right)^2 \int_{\nu_{\text{th},i}}^{\infty} \frac{B_\nu(T)}{h\nu} \sigma_P(\nu, \nu_\gamma, \mu_i) \quad (20)$$

with  $i = 1, 2$ ;  $\nu_\gamma$  denotes the  $\gamma$ -ray frequency, and  $B_\nu(T)$  the Planck function. We have to integrate over the soft photon frequency  $\nu$  above the threshold energy

$$h\nu_{\text{th},i} = \frac{2(m_e c^2)^2}{(1 - \mu_i)h\nu_\gamma}, \quad (21)$$

where  $m_e c^2$  refers to the rest-mass energy of the electron. The cosine of the collision angle  $\mu_i$  becomes  $1 - \mu_1 = 1 - \sin \theta_0$  for outward (or  $1 - \mu_2 = 1 + \sin \theta_0$  for inward)  $\gamma$ -rays. That is, collisions take place head-on (or tail-on) for inward (or outward)  $\gamma$ -rays. The total cross section is given by

$$\sigma_P = \frac{3}{16} \sigma_T (1 - v^2) \left[ (3 - v^4) \ln \frac{1 + v}{1 - v} - 2v(2 - v^2) \right], \quad (22)$$

where  $\sigma_T$  denotes the Thomson cross section and

$$v \equiv \sqrt{1 - \frac{2}{1 - \mu_i} \frac{(m_e c^2)^2}{h\nu h\nu_\gamma}}. \quad (23)$$

Pair production takes place when the  $\gamma$ -rays collide with the surface X-rays in the Wien regime, that is, at  $h\nu \gg kT$ . An accurate evaluation of  $\sigma_2$  requires a careful treatment of the collision geometry, because the threshold energy,  $h\nu_{\text{th},2}$ , strongly depends on the tiny collision angles. In the numerical method (next section), the pair-production absorption coefficient is explicitly computed at each point in the three-dimensional pulsar magnetosphere by equation (50). However, in this section, for analytical purpose, we simply adopt the empirical relation,

$$\sqrt{F_1 \sigma_1 F_2 \sigma_2} = \epsilon \sqrt{1 - \mu_1} \sigma_T F_X, \quad (24)$$

where  $\epsilon = 0.004, 0.01$ , and  $0.038$  for  $\alpha = 45^\circ, 60^\circ$ , and  $75^\circ$ , respectively;  $1 - \mu_1 \approx 2$ . The X-ray flux is evaluated at  $(r_0, \theta_0)$  such that

$$F_X = \frac{L_X}{2.82kT} \frac{1}{4\pi r_0^2}, \quad (25)$$

where  $L_X$  refers to the luminosity of photon radiation from the cooling NS surface. For a smaller  $\alpha$ , the point  $(r_2, \theta_2)$  is located in the higher altitudes, where the magnetic field lines begin to collimate along the rotation axis, deviating from the static dipole configuration. Thus, the collision angles near the light cylinder, and hence  $\sigma_2$  decreases with decreasing  $\alpha$ . The explicit value of  $\epsilon$  can be computed only numerically, solving the photon specific intensity from infrared to  $\gamma$ -ray energies in the three-dimensional pulsar magnetosphere.

The last factor,  $l_1 l_2$ , in the left-hand side of equation (19) is given by

$$l_1 l_2 = r_0^2 \cos^2 \theta_0 (\tan \theta_0 - \tan \theta_1) (\tan \theta_2 - \tan \theta_0) \quad (26)$$

Thus, equation (19) gives

$$\frac{eE_{\parallel}}{h\nu_c} \frac{L_X/c}{2.82kT} \epsilon \sqrt{1 - \mu_1} \sigma_T \times \cos^2 \theta_0 (\tan \theta_0 - \tan \theta_1) (\tan \theta_2 - \tan \theta_0) = 1, \quad (27)$$

where the  $r_0$  dependence vanishes. Substituting equations (1), (2), (3) into (27), we can solve  $h_m$  as a function of  $L_X/kT$ ,  $P$ , and  $\mu$ .

To describe the evolution of  $P = P(t) = 2\pi/\Omega(t)$ , we adopt in this paper

$$-I\Omega\dot{\Omega} = C \frac{\mu^2 \Omega^4}{c^3} \quad (28)$$

where  $C = (2/3) \sin^2 \alpha$  for a magnetic dipole braking, while  $C = 1 + \sin^2 \alpha$  for a force-free braking (Spitkovski 2006). Assuming a magnetic dipole braking, we obtain

$$P = 39.2 \text{ ms} \mu_{30} I_{45}^{-1/2} (t/10^3 \text{ years})^{1/2}, \quad (29)$$

where  $\mu_{30} \equiv \mu/(10^{30} \text{ G cm}^3)$  and  $I_{45} \equiv I/(10^{45} \text{ g cm}^2)$ . Thus, if we specify a cooling scenario,  $T = T(t)$ , equation (27) gives  $h_m$  as a function of  $t$ . Note that the  $\alpha$  dependence of the spin-down law is not essential for the present purpose; thus,  $C = 2/3$  is simply adopted. Once  $h_m = h_m(t)$  is obtained, equation (4) readily gives  $L_\gamma$  as a function of  $t$ , and hence of  $L_{\text{spin}}$ . It is worth noting that the heated polar-cap emission is relatively weak compared to the cooling NS emission, except for millisecond or middle-aged pulsars.

Let us now consider the cooling scenario. Since the mass of PSR J1614-2230 is precisely measured to be  $1.97 M_\odot$  (i.e., 1.97 solar masses), and since other three NSs (4U1700-377, B1957+20, and J1748-2021B) (Lattimer & Prakash 2001) are supposed to be heavier than  $2.0 M_\odot$ , we exclude the equation of state (EOS) that gives smaller maximum mass than  $1.95 M_\odot$ . That is, we do not consider the fast cooling scenario due to direct Urca process in a hyperon-mixed, pion-condensed, kaon-condensed, or quark-deconfined core, which gives softer EOS and hence a smaller maximum mass. Even without exotic matters, the direct Urca process may also become important in the core of a NS with the mass that is slightly less than the maximum mass. However, in the present paper, we exclude such relatively rare cases and adopt the canonical value,  $1.4 M_\odot$ , as the NS mass.

On these ground, we adopt the minimal cooling scenario (Page et al. 2004), which has no enhanced cooling that could result from any of the direct Urca processes and employs the standard EOS, APR EOS (Akmal et al. 1998). Within the minimal cooling scenario, the cooling history of a NS substantially depends on the composition of the envelope, which is defined as the uppermost layer extending from the photosphere down to a boundary where the luminosity in the envelope equals the total surface luminosity of the star. An envelope contains a strong temperature gradient and has a thickness around 100 meters. We adopt the cooling curves given in Page et al. (2004) and consider the two extreme cases: light element and heavy element envelopes. Because of the uncertainty in the modeling of neutron  $^1S_0$  (i.e., spin-singlet state) Cooper pairing temperature (as a function of neutron Fermi momentum) and proton  $^1S_0$  pairing temperature (as a function of proton Fermi momentum), the predicted  $L_X$  distributes in a ‘band’ for each chemical composition of the envelope. When a NS is younger than  $10^{4.4} \text{ yr}$ , a light element envelope (contaminated by e.g., H, He, C, or O with masses exceeding  $10^{-6} M_\odot$ ) has a higher surface temperature, and hence a greater luminosity,  $L_X$ , compared to a heavy element envelope (contaminated by light elements with masses less than  $10^{-16} M_\odot$ ), because the heat transport becomes

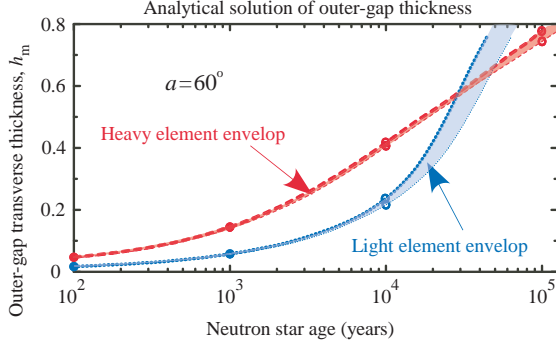


FIG. 2.— Analytically solved gap thickness. The (blue) dotted and (red) dashed curves represent  $h_m = h_m(t)$  for a light and a heavy element envelopes, respectively. Uncertainties due to nucleon Cooper pairing models, are represented by the blue and red shaded ‘bands’. Magnetic inclination angle is assumed to be  $\alpha = 60^\circ$ .

more efficient in the former. As the NS ages, a star with a light element envelope quickly loses its internal energy via photon emission; as a result, after  $10^{4.6}$  yr, it become less luminous than that with a heavy element envelope. A realistic cooling curve will be located between these two extreme cases, depending on the actual composition of the NS envelope.

We present the solved  $h_m$  for a light and a heavy element envelope in figure 2, adopting  $\mu_{30} = 3.2$ , which gives the magnetic field strength of  $4.1 \times 10^{12}$  G at the magnetic pole, where  $r_* = 11.6$  km is used. It follows that the gap becomes thinner for a light element case (between the thin and thick dotted curves, blue shaded region) than for the heavy element cases (between the thin and thick dashed curves, red shaded region). This is because the more luminous photon field of a light element envelope leads to a copious pair production, which prevents the gap to expand in the trans-field direction. As a result, the predicted  $L_\gamma$  becomes less luminous for a light element envelope than a heavy one.

In figure 3, we present the analytical results of  $L_\gamma$  versus  $L_{\text{spin}}$  as the dotted (or dashed) curve for a light (or a heavy) element envelope. As the pulsar spins down,  $L_\gamma$  evolves leftwards. In this section, for analytical purpose, we are not interested in the dependence on the observer’s viewing angle,  $\zeta$ . Thus, in equation (4), we simply put  $f_\Omega = 1$ . It is interesting to note that  $L_\gamma$  little evolves for a light element envelope, because of  $h_m \ll 1$ , as discussed after equation (11). Precisely speaking, we obtain  $h_m \propto t^{0.62}$  and hence  $L_\gamma \propto L_{\text{spin}}^{0.07}$  (or  $h_m \propto t^{0.50}$  and hence  $L_\gamma \propto L_{\text{spin}}^{0.25}$ ) for a light (or a heavy) element envelope. That is, although  $h_m$  is smaller,  $h_m$  increases more rapidly in a light element case than in a heavy element case, which enables a constant  $L_\gamma$  for a light element envelope. At later stage,  $t > 10^4$  years, both  $h_m$  and  $L_\gamma$  increase with decreasing  $L_{\text{spin}}$  for a light element envelope, because  $L_X/(kT)$ , and hence the pair production rate, rapidly decreases with increasing  $t$ . On the other hand, for a heavy element envelope, their greater  $h_m$  results in a monotonically decreasing  $L_\gamma$  with decreasing  $L_{\text{spin}}$ .

### 3. NUMERICAL EXAMINATION OF OUTER-GAP ELECTRODYNAMICS

Let us develop the analytical examination and look deeper into a self-consistent solution by a numerical

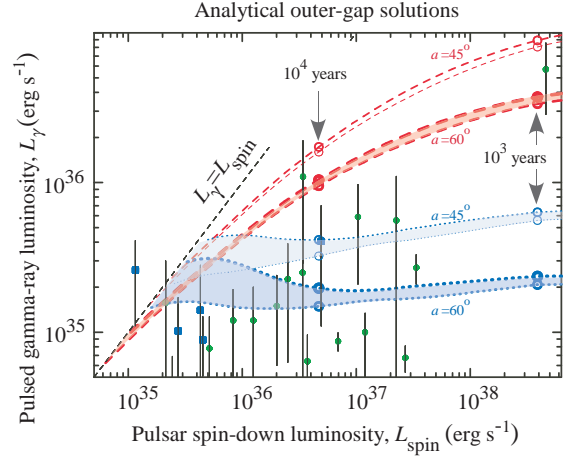


FIG. 3.— Analytically solved gap luminosity with uncertainties due to nucleon Cooper pairing models. The thick and thin dotted (or dashed) curves represent the evolution of the gap luminosity for a light (or a heavy) element envelope. Two cases of magnetic inclination angle,  $\alpha = 45^\circ$  and  $60^\circ$ , are depicted as labeled. The green filled circles designates the normal gamma-ray pulsars, while the blue filled squares do those detected by the gamma-ray blind search technique.

method. To this end, we adopt the modern outer-gap model (Hirotani 2011a) and solve the set of Maxwell and Boltzmann equations self-consistently and compute  $E_\parallel$ , distribution functions of  $e^\pm$ s, and the photon specific intensity at each point in the three-dimensional pulsar magnetosphere. We consider not only the whole-surface, cooling NS emission but also the heated polar-cap emission as the photon source of photon-photon pair production in the numerical analysis. The former emission component is given as a function of the pulsar age from the minimum cooling scenario, in the same manner as in the analytical examination, while the latter emission component is solved consistently with the energy flux of the  $e^-$ s falling on to the pulsar polar-cap surface. The method described below was also used in recent theoretical computation of the Crab pulsar’s  $\gamma$ -ray emissions (Aleksić et al. 2011a,b).

Let us present the basic equations that describe a pulsar outer-magnetospheric accelerator, extending the method first proposed for black-hole magnetospheres (Beskin 1992; Hirotani & Okamoto 1998). Around a rotating NS, the background geometry is described by the space-time metric (Lense & Thirring 1918)

$$ds^2 = g_{tt}dt^2 + 2g_{t\varphi}dtd\varphi + g_{rr}dr^2 + g_{\theta\theta}d\theta^2 + g_{\varphi\varphi}d\varphi^2, \quad (30)$$

where

$$g_{tt} \equiv \left(1 - \frac{r_g}{r}\right) c^2, \quad g_{t\varphi} \equiv ac \frac{r_g}{r} \sin^2 \theta, \quad (31)$$

$$g_{rr} \equiv -\left(1 - \frac{r_g}{r}\right)^{-1}, \quad g_{\theta\theta} \equiv -r^2, \quad g_{\varphi\varphi} \equiv -r^2 \sin^2 \theta; \quad (32)$$

$M$  denotes the NS mass,  $r_g \equiv 2GM/c^2$  the Schwarzschild radius, and  $a \equiv I\Omega/(Mc)$  the stellar angular momentum. At radial coordinate  $r$ , the inertial frame is dragged at angular frequency  $\omega \equiv -g_{t\varphi}/g_{\varphi\varphi} = 0.15\Omega I_{45} r_6^{-3}$ , where  $I_{45} \equiv I/10^{45}$  erg cm<sup>2</sup>, and  $r_6 \equiv r_*/10$  km.

First, let us derive the Poisson equation for the electrostatic potential under the space-time geometry described

just above. Let us consider the Gauss's law,

$$\nabla_\mu F^{t\mu} = \frac{1}{\sqrt{-g}} \partial_\mu \left[ \frac{\sqrt{-g}}{\rho_w^2} g^{\mu\nu} (-g_{\varphi\varphi} F_{t\nu} + g_{t\varphi} F_{\varphi\nu}) \right] = \frac{4\pi}{c^2} \rho, \quad (33)$$

where  $\nabla$  denotes the covariant derivative, the Greek indices run over  $t, r, \theta, \varphi$ ;  $\sqrt{-g} = \sqrt{g_{rr}g_{\theta\theta}\rho_w^2} = cr^2 \sin \theta$  and  $\rho_w^2 \equiv g_{t\varphi}^2 - g_{tt}g_{\varphi\varphi}$ ,  $\rho$  the real charge density. The electromagnetic fields observed by a distant static observer are given by (Camenzind 1986a,b)  $E_r = F_{rt}$ ,  $E_\theta = F_{\theta t}$ ,  $E_\varphi = F_{\varphi t}$ ,  $B^r = (g_{tt} + g_{t\varphi}\Omega)F_{\theta\varphi}/\sqrt{-g}$ ,  $B^\theta = (g_{tt} + g_{t\varphi}\Omega)F_{\varphi r}/\sqrt{-g}$ ,  $B_\varphi = -\rho_w^2 F_{r\theta}/\sqrt{-g}$ , where  $F_{\mu\nu} \equiv \partial_\mu A_\nu - \partial_\nu A_\mu$  and  $A_\mu$  denotes the vector potential.

We assume that the electromagnetic fields are unchanged in the co-rotating frame. In this case, it is convenient to introduce the non-corotational potential  $\Psi$  that satisfies

$$F_{\mu t} + \Omega F_{\mu\varphi} = -\partial_\mu \Psi(r, \theta, \varphi - \Omega t), \quad (34)$$

where  $\mu = t, r, \theta, \varphi$ . If  $F_{At} + \Omega F_{A\varphi} = 0$  holds for  $A = r$  and  $\theta$ , the magnetic field rigidly rotates with angular frequency  $\Omega$ . Imposing that the NS surface a perfect conductor,  $F_{\theta t} + \Omega F_{\theta\varphi} = 0$ , we find that the NS surface becomes equi-potential,  $\partial_\theta \Psi = \partial_t \Psi + \Omega \partial_\varphi \Psi = 0$ . However, in a particle acceleration region, the magnetic field does not rigidly rotate, because  $F_{At} + \Omega F_{A\varphi}$  deviates from 0. The deviation is expressed in terms of  $\Psi$ , which gives the strength of the acceleration electric field,

$$E_\parallel \equiv \frac{\mathbf{B}}{B} \cdot \mathbf{E} = \frac{B^i}{B} (F_{it} + \Omega F_{i\varphi}) = \frac{B}{B} \cdot (-\nabla \Psi), \quad (35)$$

which is measured by a distant static observer, where the Latin index  $i$  runs over spatial coordinates  $r, \theta, \varphi$ .

Substituting equation (34) into (33), we obtain the Poisson equation for  $\Psi$ ,

$$-\frac{c^2}{\sqrt{-g}} \partial_\mu \left( \frac{\sqrt{-g}}{\rho_w^2} g^{\mu\nu} g_{\varphi\varphi} \partial_\nu \Psi \right) = 4\pi(\rho - \rho_{\text{GJ}}), \quad (36)$$

where

$$\rho_{\text{GJ}} \equiv \frac{c^2}{4\pi\sqrt{-g}} \partial_\mu \left[ \frac{\sqrt{-g}}{\rho_w^2} g^{\mu\nu} g_{\varphi\varphi} (\Omega - \omega) F_{\varphi\nu} \right] \quad (37)$$

denotes the general relativistic Goldreich-Julian charge density. If  $\rho = \rho_{\text{GJ}}$  holds everywhere,  $E_\parallel$  vanishes in the entire region, provided that the boundaries are equi-potential. However, if  $\rho$  deviates from  $\rho_{\text{GJ}}$  in any region,  $E_\parallel$  appears around the region with differentially rotating magnetic field lines. In the higher altitudes,  $r \gg r_g$ , equation (37) reduces to the special-relativistic expression (Goldreich, & Julian 1969; Mestel 1971),

$$\rho_{\text{GJ}} \equiv -\frac{\mathbf{\Omega} \cdot \mathbf{B}}{2\pi c} + \frac{(\mathbf{\Omega} \times \mathbf{r}) \cdot (\nabla \times \mathbf{B})}{4\pi c}, \quad (38)$$

which is commonly used.

Instead of  $(r, \theta, \varphi)$ , we adopt the magnetic coordinates  $(s, \theta_*, \varphi_*)$ , where  $s$  denotes the distance along a magnetic field line,  $\theta_*$  and  $\varphi_*$  represents the magnetic colatitude and the magnetic azimuthal angle, respectively, of the point where the field line intersects the NS surface. Defining that  $\theta_* = 0$  corresponds to the magnetic axis and that  $\varphi_* = 0$  to the latitudinal plane on which

both the rotation and the magnetic axes reside, we obtain the Poisson equation (Hirotani 2006a,b),

$$\begin{aligned} & -\frac{c^2 g_{\varphi\varphi}}{\rho_w^2} (g^{ss} \partial_s^2 + g^{\theta_*\theta_*} \partial_{\theta_*}^2 + g^{\varphi_*\varphi_*} \partial_{\varphi_*}^2 \\ & + 2g^{s\theta_*} \partial_s \partial_{\theta_*} + 2g^{\theta_*\varphi_*} \partial_{\theta_*} \partial_{\varphi_*} + 2g^{\varphi_*s} \partial_{\varphi_*} \partial_s) \Psi \\ & - (A^s \partial_s + A^{\theta_*} \partial_{\theta_*} + A^{\varphi_*} \partial_{\varphi_*}) \Psi = 4\pi(\rho - \rho_{\text{GJ}}), \end{aligned} \quad (39)$$

where

$$\begin{aligned} g^{i'j'} &= g^{\mu\nu} \frac{\partial x^{i'}}{\partial x^\mu} \frac{\partial x^{j'}}{\partial x^\nu} = g^{rr} \frac{\partial x^{i'}}{\partial r} \frac{\partial x^{j'}}{\partial r} + g^{\theta\theta} \frac{\partial x^{i'}}{\partial \theta} \frac{\partial x^{j'}}{\partial \theta} \\ & - \frac{k_0}{\rho_w^2} \frac{\partial x^{i'}}{\partial \varphi} \frac{\partial x^{j'}}{\partial \varphi}, \end{aligned} \quad (40)$$

$$\begin{aligned} A^{i'} &\equiv \frac{c^2}{\sqrt{-g}} \left\{ \partial_r \left[ \frac{g_{\varphi\varphi}}{\rho_w^2} \sqrt{-g} g^{rr} \frac{\partial x^{i'}}{\partial r} \right] \right. \\ & \left. + \partial_\theta \left[ \frac{g_{\varphi\varphi}}{\rho_w^2} \sqrt{-g} g^{\theta\theta} \frac{\partial x^{i'}}{\partial \theta} \right] \right\} - \frac{c^2 g_{\varphi\varphi}}{\rho_w^2} \frac{k_0}{\rho_w^2} \frac{\partial^2 x^{i'}}{\partial \varphi^2}; \end{aligned} \quad (41)$$

the coordinate variables are  $x^1 = r$ ,  $x^2 = \theta$ ,  $x^3 = \varphi$ ,  $x^{1'} = s$ ,  $x^{2'} = \theta_*$ , and  $x^{3'} = \varphi_*$ . Note that this formalism is applicable to arbitrary magnetic field configurations, and also that equation (35) gives  $E_\parallel = -(\partial\Psi/\partial s)_{\theta_*, \varphi_*}$ . Causality requires that a plasmas can co-rotate with the magnetic field only in the region that satisfies  $k_0 \equiv g_{tt} + 2g_{t\varphi}\Omega + g_{\varphi\varphi}\Omega^2 > 0$  (Znajek 1977; Takahashi et al. 1990). That is, the concept of the light cylinder is generalized into the light surface on which  $k_0$  vanishes. The effects of magnetic field expansion (Scharlemann et al. 1978; Muslimov & Tsygan 1992) are contained in the coefficients of the trans-field derivatives,  $g^{\theta_*\theta_*}$ ,  $g^{\theta_*\varphi_*}$ ,  $g^{\varphi_*\varphi_*}$ . In what follows, we adopt the vacuum, rotating dipole solution (Cheng et al. 2000) to describe the magnetic field configuration.

Second, let us consider the particle Boltzmann equations. At time  $t$ , position  $\mathbf{r}$ , and momentum  $\mathbf{p}$ , they become,

$$\frac{\partial N_\pm}{\partial t} + \mathbf{v} \cdot \nabla N_\pm + \left( q\mathbf{E} + \frac{\mathbf{v}}{c} \times \mathbf{B} \right) \cdot \frac{\partial N_\pm}{\partial \mathbf{p}} = S_\pm(t, \mathbf{r}, \mathbf{p}), \quad (42)$$

where  $N_+$  (or  $N_-$ ) denotes the positronic (or electronic) distribution function;  $\mathbf{v} \equiv \mathbf{p}/(m_e \gamma)$ ,  $m_e$  refers to the rest mass of the electron, and  $q$  the charge on the particle. The Lorentz factor is given by  $\gamma \equiv 1/\sqrt{1 - (|\mathbf{v}|/c)^2}$ . The collision term  $S_+$  (or  $S_-$ ) consists of the terms that represent the appearing and disappearing rates of positrons (or electrons) at  $\mathbf{r}$  and  $\mathbf{p}$  per unit time per unit phase-space volume. Since we are dealing with high-energy phenomena, we consider wave frequencies that are much greater than the plasma frequency and neglect the collective effects.

It is noteworthy that the particle flux per magnetic flux tube is conserved along the flow line if there is no particle creation or annihilation. Thus, it is convenient to normalize the particle distribution functions by the Goldreich-Julian number density such that  $n_\pm = \langle N_\pm \rangle / (\Omega B / 2\pi c e)$ , where  $\langle \rangle$  denotes that the quantity is averaged in a gyration. Imposing a stationary condition

$\partial/\partial t + \Omega\partial/\partial\phi = 0$  in the co-rotating frame, we can reduce the particle Boltzmann equations into (Hirotani et al. 2003)

$$c \cos \chi \frac{\partial n_{\pm}}{\partial s} + \dot{p} \frac{\partial n_{\pm}}{\partial p} + \dot{\chi} \frac{\partial n_{\pm}}{\partial \chi} = S_{\text{IC}} + S_{\text{p}}, \quad (43)$$

where the upper and lower signs correspond to the positrons (with charge  $q = +e$ ) and electrons ( $q = -e$ ), respectively,  $\chi$  denotes the pitch angle of gyrating particles, and  $p \equiv |\mathbf{p}| = m_e c \sqrt{\gamma^2 - 1}$ . Since pair annihilation is negligible in a pulsar magnetosphere,  $S_{\pm}$  consists of the IC scattering term,  $S_{\text{IC}}$ , and the pair creation term,  $S_{\text{p}}$ , in the right-hand side. When a particle emits a photon via synchro-curvature process, the energy loss ( $\sim \text{GeV}$ ) is small compared to the particle energy ( $\sim 10 \text{ TeV}$ ); thus, it is convenient to include the back reaction of the synchro-curvature emission as a friction term in the left-hand side (Hirotani 2006a). In this case, the characteristics of equation (43) in the phase space are given by

$$\dot{p} \equiv qE_{\parallel} \cos \chi - \frac{P_{\text{SC}}}{c}, \quad (44)$$

$$\dot{\chi} \equiv -\frac{qE_{\parallel} \sin \chi}{p} + c \frac{\partial(\ln B^{1/2})}{\partial s} \sin \chi, \quad (45)$$

where the synchro-curvature radiation force,  $P_{\text{SC}}/c$  (Cheng & Zhang 1996; Zhang & Cheng 1997), is included as the friction; the particle position  $s$  is related with time  $t$  by  $\dot{s} = ds/dt = c \cos \chi$ . For outward- (or inward-) migrating particles,  $\cos \chi > 0$  (or  $\cos \chi < 0$ ). If  $E_{\parallel} = 0$ , particles will be reflected by magnetic mirrors, which are expressed by the second term in the right-hand side of equation (45). If we integrate  $n_{\pm}$  over  $p$  and  $\chi$ , and multiply the local GJ number density,  $\Omega B/2\pi ce$ , we obtain the spatial number density of particles. Therefore, we can express the real charge density  $\rho$  as

$$\rho = \frac{\Omega B}{2\pi c} \iint (n_{+} - n_{-}) d\gamma d\chi + \rho_{\text{ion}}, \quad (46)$$

where  $n_{\pm}$  are a function of  $s, \theta, \varphi, \gamma, \chi$ ;  $\rho_{\text{ion}}$  refers to the charge density of ions, which can be drawn from the NS surface as a space-charge-limited flow (SCLF) by a positive  $E_{\parallel}$  (Hirotani 2006a).

In equation (43), the collision terms are expressed as

$$S_{\text{IC}} \equiv - \sum_n^{\epsilon_{n-1} < \gamma} \eta_{\text{IC}}^{\gamma}(\langle \epsilon_n \rangle, \gamma, \mu_c) \iint n_{\pm} d\gamma d\chi, \\ + \sum_i \eta_{\text{IC}}^e(\gamma_i, \gamma, \mu_c) \iint n_{\pm} d\gamma d\chi, \quad (47)$$

and

$$S_{\text{p}} \equiv \frac{2\pi ce}{\Omega B} \int (\alpha_{\gamma B} + \alpha_{\gamma\gamma}) \int \frac{I_{\nu}}{h\nu} d\tilde{\omega} d\nu, \quad (48)$$

where  $\langle \epsilon_n \rangle = (\epsilon_{n-1} + \epsilon_n)/2$  represents the typical photon energy within the interval  $[m_e c^2 \epsilon_{n-1}, m_e c^2 \epsilon_n]$ ,  $\mu_c$  the cosine of the collision angle between the particles and the soft photons,  $I_{\nu}$  the specific intensity of the radiation field,  $\tilde{\omega}$  the solid angle into which the photons are propagating. To compute  $S_{\text{p}}$  at each point, we have to integrate  $I_{\nu}/(h\nu)$  in all directions to calculate the differential photon number flux,  $\int I_{\nu}/(h\nu) d\tilde{\omega}$ . The absorption

coefficients for magnetic and photon-photon pair production processes, are given by

$$\alpha_{\gamma B} = \frac{e^2/\hbar c}{4.4} \frac{m_e c}{h} B'_{\perp} \exp\left(-\frac{8}{3} \frac{1}{\epsilon_{\gamma} B'_{\perp}}\right) \\ \times \delta(\gamma - \gamma_0) \delta(\chi - \chi_0), \quad (49)$$

$$\alpha_{\gamma\gamma} = \frac{1 - \cos \theta_c}{2} \int_{\epsilon_{\text{th}}}^{\infty} d\epsilon_s \frac{dF_s}{d\epsilon_s} \frac{\partial^2 \sigma_{\gamma\gamma}}{d\gamma d\chi}, \quad (50)$$

where  $B'_{\perp} \equiv B \sin \theta_c / B_{\text{cr}}$ ; explicit expression of  $\eta_{\text{IC}}^{\gamma}$  and  $\partial^2 \sigma_{\gamma\gamma}/d\gamma d\chi$  are given in the literature (e.g., Hirotani et al. (2003)). In equation (49),  $B'_{\perp}$  contains the collision angle,  $\theta_c$ , between the photon and the magnetic field. In equation (50),  $\theta_c$  does that between the two photons. The IC redistribution function  $\eta_{\text{IC}}^{\gamma}(\epsilon_{\gamma}, \gamma, \mu_c)$  represents the probability that a particle with Lorentz factor  $\gamma$  up-scatters photons into energies between  $m_e c^2 \epsilon_{\gamma}$  and  $m_e c^2 (\epsilon_{\gamma} + d\epsilon_{\gamma})$  per unit time when the collision angle is  $\cos^{-1} \mu_c$ , where  $\epsilon_{\gamma} = h\nu/(m_e c^2)$  refers to the dimensionless photon energy. On the other hand,  $\eta_{\text{IC}}^e(\gamma_i, \gamma_f, \mu_c)$  represents the probability for a particle to change its Lorentz factor from  $\gamma_i$  to  $\gamma_f$  in a single scattering. We thus obtain  $\eta_{\text{IC}}^e(\gamma_i, \gamma_f, \mu_c) = \eta_{\text{IC}}^{\gamma}(\gamma_i - \gamma_f, \gamma_i, \mu_c)$  by energy conservation.

Third, let us consider the radiative transfer equation. The variation of specific intensity,  $I_{\nu}$ , along a ray is described by the radiative transfer equation,

$$\frac{dI_{\nu}}{dl} = -\alpha_{\nu} I_{\nu} + j_{\nu}, \quad (51)$$

where  $l$  refers to the distance along the ray,  $\alpha_{\nu}$  and  $j_{\nu}$  the absorption and emission coefficients, respectively. Both  $\alpha_{\nu}$  and  $j_{\nu}$  are a function of  $l$ , photon energy  $E_{\gamma}$ , and propagation direction  $(k^{\theta}, k^{\varphi})$ , where  $k^{\mu}$  denotes the photon momentum four vector ( $\mu = t, r, \theta, \varphi$ ).

Equation (51) can be solved if we specify the photon propagation in the curved space time. The evolution of momentum and position of a photon is described by the Hamilton-Jacobi equations,

$$c \frac{dk_r}{dl} = -\frac{\partial k_t}{\partial r}, \quad c \frac{dk_{\theta}}{dl} = -\frac{\partial k_t}{\partial \theta}, \quad (52)$$

$$c \frac{dr}{dl} = \frac{\partial k_t}{\partial k_r}, \quad c \frac{d\theta}{dl} = \frac{\partial k_t}{\partial k_{\theta}}. \quad (53)$$

Since the metric (eqs. [30]–[32]) is stationary and axisymmetric, the photon energy at infinity  $k_t$  and the azimuthal wave number  $-k_{\varphi}$  are conserved along the ray. When a particle is rotating with angular velocity  $\dot{\varphi}$  and emit a photon with energy  $E_{\text{local}}$ ,  $k_t$  and  $-k_{\varphi}$  are related to these quantities by the redshift relation,  $E_{\text{local}} = (dt/d\tau)(k_t + k_{\varphi}\dot{\varphi})$ , where  $dt/d\tau$  is solved from the definition of the proper time,  $(dt/d\tau)^2 (g_{tt} + 2g_{t\varphi}\dot{\varphi} + g_{\varphi\varphi}\dot{\varphi}^2) = 1$ . The dispersion relation  $k^{\mu}k_{\mu} = 0$ , which is quadratic to  $k_{\mu}$ 's ( $\mu = t, r, \theta, \varphi$ ), gives Hamiltonian  $k_t$  in terms of  $r, \theta, k_r, k_{\theta}$ , and  $k_{\varphi}$ . Thus, we have to solve the set of four ordinary differential equations (52) and (53) for  $k_r, k_{\theta}, r$ , and  $\theta$ . When photons are emitted, they are highly beamed along the particle's motion; thus, the initial conditions of  $(k^r, k^{\theta}, k^{\varphi})$  are given by the instantaneous particle's velocity measured by a distant static observer. It may be helpful to give the initial conditions of ray tracing in the limit  $r \gg r_g$  and  $\gamma \gg 1$ , because photons are



emitted mostly in the outer magnetosphere. In this limit, the orthonormal components of the  $e^+$ 's and  $e^-$ 's instantaneous velocity are given by (Mestel 1985; Camenzind 1986a,b)

$$\frac{v^r}{c} = f_v \frac{B^r}{c}, \quad \frac{v^{\hat{\theta}}}{c} = f_v \frac{B^{\hat{\theta}}}{c}, \quad \frac{v^{\hat{\phi}}}{c} = f_v \frac{B^{\hat{\phi}}}{c} + \frac{\varpi}{\varpi_{\text{LC}}} \quad (54)$$

in the polar coordinates, where

$$f_v \equiv -\frac{\varpi}{\varpi_{\text{LC}}} \frac{B^{\hat{\phi}}}{B} \pm \sqrt{1 - \left(\frac{\varpi}{\varpi_{\text{LC}}}\right)^2 \left(\frac{B_p}{B}\right)^2}; \quad (55)$$

$B_p \equiv \sqrt{(B^r)^2 + (B^{\hat{\theta}})^2}$ . The upper (or the lower) sign of  $f_v$  (eq. [55]) corresponds to the outward (or the inward) particle velocity. Note that  $B^{\hat{\phi}} < 0$  holds in ordinary situation.

Fourth and finally, let us impose appropriate boundary conditions to solve the set of Maxwell (i.e., Poisson) and Boltzmann equations. We start with considering the boundary conditions for the elliptic type equation (36). We define that the *inner* boundary,  $s = 0$ , coincides with the NS surface, on which we put  $\Psi = 0$  for convenience. The *outer* boundary,  $s = s_{\text{out}}(\theta_*, \varphi_*)$ , is defined as the place where  $E_{\parallel}$  changes sign near the light cylinder. Its location is solved self-consistently as a free-boundary problem and appears near the place where  $\partial(\rho_{\text{GJ}}/B)/\partial s$  vanishes due to the flaring up of the field lines towards the rotation axis (eq. [68] of Hirotani (2006a)). At each  $\varphi_*$ , the *lower* boundary  $\theta_* = \theta_*^{\text{max}}(\varphi_*)$  is assumed to coincide with the last open field line, which is defined by the condition that  $\sqrt{-g_{rr}}B^r \sin\theta + \sqrt{-g_{\theta\theta}}B^{\theta} \cos\theta = 0$  is satisfied at the light cylinder. We can compute the potential drop along each field line,  $\Delta\Psi(\theta_*, \varphi_*) \equiv \Psi(s = 0) - \Psi(s = s_{\text{out}}) = -\Psi(s = s_{\text{out}})$ , by integrating  $E_{\parallel}$  along the field line. The maximum value of  $\Delta\Psi(\theta_*, \varphi_*)$  is referred to as  $\Delta\Psi_{\text{max}}$ .

Let us consider the *upper* boundary,  $\theta_*^{\text{min}} = \theta_*^{\text{min}}(s, \varphi_*)$ . At each  $(s, \varphi_*)$ ,  $E_{\parallel}$  vanishes on the last-open field line,  $\theta_* = \theta_*^{\text{max}}$  (i. e., at the lower boundary), and increases with decreasing  $\theta_*$  in the latitudinal direction (i. e., towards the magnetic axis). The acceleration field  $E_{\parallel}$  peaks around the middle-latitudes,  $\theta_* \approx [\theta_*^{\text{max}} + \theta_*^{\text{min}}]/2 = (1 - h_m/2)\theta_*^{\text{max}}$ , and turns to decrease towards the upper boundary. At some co-latitude,  $E_{\parallel}$  eventually decreases below  $0.01\Delta\Psi_{\text{max}}/\varpi_{\text{LC}}$ ; we define this co-latitude as the gap upper boundary,  $\theta_*^{\text{min}} = \theta_*^{\text{min}}(s, \varphi_*)$ . To specify the magnetic field line at each  $\varphi_*$ , it is convenient to introduce the dimensionless co-latitude,

$$h \equiv 1 - \theta_*/\theta_*^{\text{max}}(\varphi_*). \quad (56)$$

For example,  $h = 0$  specifies the last-open field line, and  $h = 0.1$  does the field line having the foot point on the polar-cap (PC) surface at  $\theta_* = 0.9\theta_*^{\text{max}}$  at each magnetic azimuthal angle  $\varphi_*$ . At the upper boundary, we obtain

$$h = h_m(s, \varphi_*) \equiv 1 - \theta_*^{\text{min}}(s, \varphi_*)/\theta_*^{\text{max}}(\varphi_*). \quad (57)$$

To solve the Poisson equation, we put  $\Psi = 0$  at  $h = h_m$ , or equivalently, at  $\theta_* = \theta_*^{\text{min}}(s, \varphi_*)$ . If  $h_m \ll 1$ , the gap becomes thin, whereas  $h_m \sim 1$  indicates that the gap is threaded by most of the open-field lines. Note that

the open field lines cross the PC surface at magnetic co-latitudes  $\theta_*^{\text{min}} = (1 - h_m)\theta_*^{\text{max}} < \theta_* = (1 - h)\theta_*^{\text{max}} < \theta_*^{\text{max}}$  (i.e.,  $h_m > h > 0$ ), and that  $\theta_* = 0$  (i.e.,  $h = 1$ ) corresponds to the magnetic axis.

We also have to consider the boundary conditions for the hyperbolic type equations (43) and (51). (Eq. [51] itself is an ordinary differential equation; however, it is equivalent to solving the Boltzmann equation of photon distribution function.) We assume that  $e^{\pm}$ 's and photons are not injected into the gap across either the inner or the outer boundaries. However, if the created current becomes greater than the GJ value, a positive  $E_{\parallel}$  arises at the NS surface to draw ions from the surface as a SCLF until  $E_{\parallel}$  almost vanishes at the surface.

To sum up, we solve the set of partial and ordinary differential equations (36), (43), and (51) under the boundary conditions described in the three foregoing paragraphs. By this method, we can solve the acceleration electric field  $E_{\parallel}$ , particle distribution functions  $n_{\pm}$ , and the photon specific intensity  $I_{\nu}$  (from  $h\nu = 0.005$  eV to 50 TeV), at each position in the three-dimensional magnetosphere of arbitrary rotation-powered pulsars, if we specify  $P$ ,  $\mu$ ,  $\alpha$ , and  $kT$ , where the surface temperature  $kT$  is necessary to compute the photon-photon pair production through the differential flux  $dF_s/d\epsilon_s$  in equation (50). We adopt the minimum cooling scenario in the same manner as in § 2.

In figure 4, we plot the result of  $L_{\gamma}$  as a function of  $L_{\text{spin}}$  as the dash-dotted (or solid) curve for a light (or a heavy) element envelope, where  $\mu_{30} = 3.2$  is adopted in the same manner as in the analytical examination. It follows that these numerical solutions are consistent with the analytical ones, and that  $L_{\gamma}$  decreases slowly until  $10^{4.5}$  years. The physical reason why  $L_{\gamma}$  increases with decreasing  $L_{\text{spin}}$  at  $t > 10^4$  years for a light element envelope, is the same as described at the end of § 2. A realistic NS will have an envelope composition between the two extreme cases, light and heavy elements. Thus, the actual  $L_{\gamma}$ 's will distribute between the red solid (or dashed) and the blue dash-dotted (or dotted) curves. However, after  $L_{\gamma}$  approaches  $L_{\text{spin}}$  (thin dashed straight line; see Wang & Hirotani (2011) for the death line argument), the outer gap survives only along the limited magnetic field lines in the trailing side of the rotating magnetosphere because of a less efficient pair production; as a result,  $L_{\gamma}$  rapidly decreases with decreasing  $L_{\text{spin}}$ . For a smaller  $\alpha$ , even for a light element envelope,  $L_{\gamma}$  monotonically decreases as the dash-dot-dot-dot curve shows, because the gap is located in the higher altitudes, and because the less efficient pair production there prevents the produced electric current to increase with decreasing age around  $t \sim 10^{4.5}$  years.

#### 4. EXPONENTIAL CUTOFF ENERGY

It is also worth examining the cutoff energy,  $E_{\text{cutoff}}$ , of the gamma-ray spectrum. We plot  $E_{\text{cutoff}}$  as a function of the magnetic-field strength at the light cylinder,  $B_{\text{LC}}$ , in figure 5. In the analytical computation (dash, dotted, and dash-dot-dot-dot curves), only the curvature process (Hirotani 2011a) from the particles produced and accelerated in the outer gap, is considered as the photon emission process, and no photon absorption is considered. In the numerical computation (solid and dash-



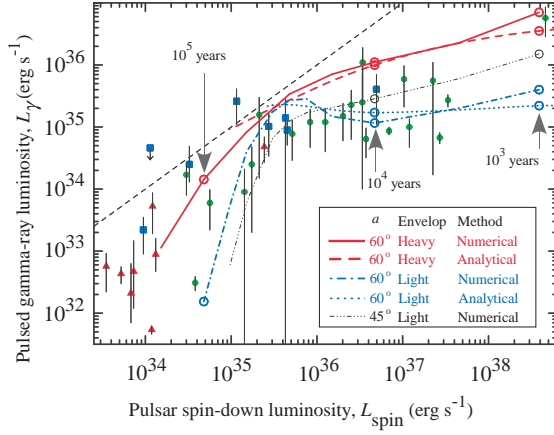


FIG. 4.— Same figure as figure 3, but numerical results are plotted as dash-dotted and solid curves for a light and a heavy element envelope, respectively. For comparison, a numerical solution for  $\alpha = 45^\circ$  and a light element envelope, is also plotted as the dash-dot-dot-dot curve. To avoid complications, we adopt the geometrical mean of the upper-bound  $L_X$  and lower-bound  $L_X$  of cooling curves for each chemical composition, instead of depicting a ‘band’, which reflects the uncertainties in the nucleon Cooper pairing models.

dotted curves), on the other hand, synchro-curvature and inverse-Compton processes from the particles not only produced and accelerated in the gap but also cascaded outside the gap, are considered as the emission processes, and both the photon-photon and magnetic pair production processes are taken into account when computing the photon propagation. Therefore, for very young pulsars, a strong photon-photon absorption (and the subsequent production of lower-energy photons via synchrotron and synchrotron-self-Compton processes) takes place even in the higher altitudes. As a result, spectrum can no longer be fitted by power-law with exponential-cutoff functional form. Thus, for  $t < 10^4$  years, the fitted cutoff energies are not plotted for numerical solutions (i.e., solid and dash-dotted curves).

It follows that the present outer gap model explains the observed tendency that  $E_{\text{cutoff}}$  increases with increasing  $B_{\text{LC}}$ , because the Goldreich-Julian charge density (in the gap) increases with increasing  $B_{\text{LC}}$ . It also follows that  $E_{\text{cutoff}}$  is regulated below several GeV, because copious pair production leads to  $h_m \ll 1$  for young pulsars (i.e., for strong  $B_{\text{LC}}$ ).

##### 5. FLUX CORRECTION FACTOR

Finally, let us investigate the flux correction factor,  $f_\Omega$ . To infer the  $\gamma$ -ray luminosity,  $L_\gamma = 4\pi f_\Omega F_\gamma d^2$ , from the observed flux,  $F_\gamma$ , one has conventionally assumed that the flux conversion factor is approximately unity,  $f_\Omega \approx 1$ , where  $d$  denotes the distance to the pulsar. However, now we can compute  $f_\Omega$  explicitly as a function of the observer’s viewing angle,  $\zeta$ , using the three-dimensional numerical solution. In figure 6,  $f_\Omega(\zeta)$  is depicted for heavy and light element envelopes at  $10^4$  and  $10^5$  years. It follows that the error of  $f_\Omega = 1$  is kept within a factor of 3 with a probability greater than 50%. When the pulsar is young,  $E_\parallel$  is highly screened in the middle and lower altitudes; as a result, most  $\gamma$ -rays are emitted from the higher altitudes to appear within the observer’s viewing angle  $46^\circ < \zeta < 53^\circ$  (i.e.,  $0.6 < \cos \zeta < 0.7$ ). However, as the pulsar ages, more  $\gamma$ -rays are emitted from

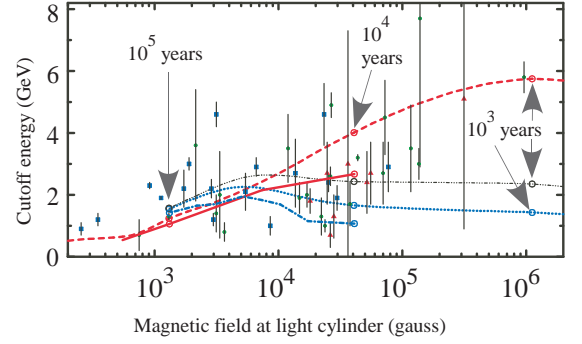


FIG. 5.— Cutoff energy of  $\gamma$ -ray spectrum. The dashed and dotted curves denote the cutoff energies obtained analytically for heavy and light element envelopes, respectively, whereas the solid and dash-dotted curves do those obtained numerically for heavy and light element envelopes, respectively. For these four cases,  $\alpha = 60^\circ$  is assumed. For comparison, an analytical solution for  $\alpha = 45^\circ$  and a light element envelope, is also plotted as the dash-dot-dot-dot curve.

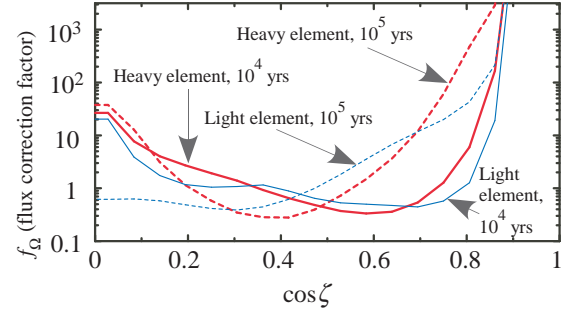


FIG. 6.— Flux correction factor,  $f_\Omega$ , as a function of the observer’s viewing angle,  $\zeta$ , with respect to the rotation axis. The (red) thick solid and dashed curves denote  $f_\Omega$  at pulsar age  $10^4$  and  $10^5$  years, respectively, for a heavy element envelope, whereas the (blue) thin solid and dashed curves do those at  $10^4$  and  $10^5$  years, respectively, for a light element envelope. The abscissa denotes the cosine of  $\zeta$ ; thus,  $\zeta$  distributes randomly along the abscissa with uniform probability. For all the cases,  $\alpha = 60^\circ$  is assumed.

the middle and lower altitudes, resulting in a stronger flux near the rotational equator,  $66^\circ < \zeta < 73^\circ$ .

##### 6. DISCUSSION

To sum up, a light element envelope approximately corresponds to the lower bound of the (observationally inferred) gamma-ray luminosity of rotation-powered pulsars, whereas a heavy element one to the upper bound. The scatter of the intrinsic gamma-ray luminosity is physically determined by the magnetic inclination angle,  $\alpha$ , and the envelope composition. The cutoff energy of the primary curvature emission is kept below several GeV even for young pulsars, because the gap trans-field thickness, and hence the acceleration electric field, is suppressed by the polarization of the produced pairs in the lower altitudes.

To convert the observed  $\gamma$ -ray flux into luminosity,  $L_\gamma$ , one has conventionally assumed  $f_\Omega = 1$ . For example, the error bars of the observational data points in figure 4, do not contain any uncertainties incurred by  $f_\Omega$ . Nevertheless, if  $\alpha$  and  $\zeta$  can be constrained, we can estimate  $L_\gamma$  more accurately, by applying the present quantitative outer-gap calculations. It is noteworthy that  $L_\gamma$ ’s given in figures 3 and 4 little depend on the NS magnetic moment,  $\mu$ . This is particularly true for a light element case, which has  $h_m \ll 1$ , by the reason described after

equation (11). What is more, with an additional determination of  $d$  (e.g., by parallax observations), we can infer the composition of individual NS envelopes, by using the constrained flux correction factor,  $f_{\Omega}$  (fig. 6). We hope to address such a question as the determination of  $\alpha$  and  $\zeta$ , and hence  $f_{\Omega}$ , for individual pulsars, by making an ‘atlas’ of the pulse profiles and phase-resolved spectra that are solved from the basic equations in a wide parameter space of  $P$ ,  $\mu$ ,  $T$ ,  $\alpha$ , and  $\zeta$ , and by comparing the atlas with the observations.

The author is indebted to Dr. A. K. Harding for valuable discussion on the results. He also thanks ASPEN Center for Physics for providing precious opportunity to debate the main topic of this letter. This work is partly supported by the Formosa Program between National Science Council in Taiwan and Consejo Superior de Investigaciones Científicas in Spain administered through grant number NSC100-2923-M-007-001-MY3.

## REFERENCES

- Abdo, A. A. et al., 2010, *ApJS*, 187, 460  
 Aharonian, F. A., Bogovalov, S. V. & Khangulyan, D. 2012, *Nature* 482, 507  
 Akmal, A., Pandharipande, V. R. & Ravenhall, D. G. 1998, *Phys. Rev. C* 58, 1804  
 Aleksić, J. et al. 2011a, *ApJ* 742, 43  
 Aleksić, J., et al. 2011b, *A&A* 540, 69  
 Aliu, E. Arlen, T., Aune, T., et al. 2011, *Science* 334, 69  
 Atwood, W. B. et al. 2009, *ApJ* 697, 1071  
 Bai, X. N. & Spitkovski, A. 2010a, *ApJ* 715, 1270  
 Bai, X. N. & Spitkovski, A. 2010b, *ApJ* 715, 1282  
 Beskin, V., Ishtomin, Ya. N. & Par’ev, V. I. 1992, *Soviet Astron.* 36, 642  
 Camenzind, M. A. 1986a, *A&A* 156, 137  
 Camenzind, M. A. 1986b, *A&A* 162, 32  
 Cheng, K. S., Ho, C. & Ruderman, M. 1986a, *ApJ* 300, 500  
 Cheng, K. S., Ho, C. & Ruderman, M. 1986b, *ApJ* 300, 522  
 Cheng, K. S., Ruderman, M. & Zhang, L. 2000, *ApJ* 537, 964  
 Cheng, K. S. & Zhang, L. 1996, *ApJ* 463, 271  
 Chiang, J. & Romani, R. W. 1992, *ApJ* 400, 629  
 Daugherty, J. K. & Harding, A. K. 1982, *ApJ* 252, 337  
 Dermer, C. D. & Sturmer, S. J. 1994, *ApJ* 420, L75  
 Goldreich, P. & Julian, W. H. 1969, *ApJ* 157, 869  
 Harding, A. K., Tademaru, E. & Esposito, L. S. 1978, *ApJ* 225, 226  
 Hirotani, K. 2006a, *ApJ* 652, 1475  
 Hirotani, K. 2006b, *Mod. Phys. Lett. A* (Brief Review) 21, 1319  
 Hirotani, K. 2008, *ApJ* 688, L25  
 Hirotani, K. 2011a, The first session of the Sant Cugat Forum Astrophysics (eds Rea, N. & Torres, D. F.) p. 117 (Springer, Berlin)  
 Hirotani, K. 2011b, *ApJ* 733, L49  
 Hirotani, K. & Okamoto, I. 1998, *ApJ* 497, 563  
 Hirotani, K., Harding, A. K. & Shibata, S. 2003, *ApJ* 591, 334  
 Lattimer, J. M. & Prakash, M. 2001, *ApJ* 550, 426  
 Lense, J. & Thirring, H. 1918, *Phys. Z.* 19, 156, Translated by Mashhoon, B., Hehl, F.W. & Theiss D.S. 1984, *Gen. Relativ. Gravit.* 16, 711.  
 Mestel, L. 1971, *Nature Phys. Sci.* 233, 149  
 Mestel, L. et al. 1985, *MNRAS* 217, 443  
 Muslimov, A. G. & Tsygan, A. I. 1992, *MNRAS* 255, 61  
 Muslimov, A. & Harding, A. K. 2004, *ApJ* 606, 1143  
 Nolan, P. et al. *Fermi* Large Area Telescope second source catalog *Astroph. J. Suppl.* **199**, 31 (2012).  
 Page, D., Lattimer, J. M., Prakash, M. & Steiner A. W. 2004, *ApJS* 155, 623  
 Petri, J. 2011, *MNRAS* 412, 1870  
 Romani, R. W. 1996, *ApJ* 470, 469  
 Romani, R. & Watters, K. P. 2010, *ApJ* 714, 810  
 Scharlemann, E. T., Arons, J. & Fawley, W. T. 1978, *ApJ* 222, 297  
 Spitkovsky, A. 2006, *ApJ* 648, L51  
 Takahashi, M. et al. 1990, *ApJ* 363, 206  
 Takata, J., Shibata, S., & Hirotani, K. 2004, *MNRAS* 354, 1120  
 Takata, J., Shibata, S., Hirotani, K., and Chang, H.-K. 2006, *MNRAS* 366, 1310  
 Takata, J., Chang, H.-K., & Shibata, S. 2008, *MNRAS* 386, 748  
 Takata, J., Wang, Y. & Cheng, K. S. 2010, *ApJ* 715, 1318  
 Thompson, D. J. in *Cosmic Gamma-Ray Sources* (eds Cheng, K. S. & Romero, G. E.) 149 (*Astrophys. Space Sci. Lib.* 304, Dordrecht, Kluwer, 2004).  
 Venter, C., Harding, A. K. & Guillemot, L. 2009, *ApJ* 707, 800  
 Wang, R. B. & Hirotani, K. 2011, *ApJ* 736, 127  
 Wang, Y., Takata, J. & Cheng, K. S. 2011, *MNRAS* 414, 2664  
 Yuki, S. & Shibata, S. 2012, *PASJ* 64, 43  
 Zhang, J. L. & Cheng, K. S. 1997, *ApJ* 487, 370  
 Znajek, R. L. 1977, *MNRAS* 179, 457